A Direct Convergence Method for Computing Synthetic Seismograms for a Layered Half-Space with Sources and Receivers at Close Depths

Dengda Zhu[1,2], Tao Xu[*1,2], Jinlai Hao[2,3], and Zhenxing Yao[3]

ABSTRACT

This study presents the direct convergence method (DCM), a novel numerical method for efficient computation of synthetic seismograms in a layered half-space when sources and receivers are at close depths. Conventional methods such as the discrete wavenumber method suffer from the slow convergence in such scenarios, which requires impractical wavenumber cutoffs. Although the semi-analytical method (SAM) and peak-trough averaging method (PTAM) offer improvements, SAM involves complex mathematical derivations, and PTAM demands an extra meticulous numerical implementation. DCM addresses these limitations by directly removing the slowly convergent component of the wavenumber-domain integrand over a finite interval and supplementing it with an analytically derived correction term. The method achieves higher accuracy and better stability than PTAM with minimal computational overhead—implementable in fewer than 20 lines of code in frameworks like PyGRT. Validation via the Sommerfeld integral and Lamb's problem confirms DCM's robustness and accuracy. Applications to soft sedimentary layers and far-field scenarios demonstrate its reliability. DCM provides a simple, efficient, and easily implementable solution for high-fidelity synthetic seismograms in challenging source–receiver configurations.

KEY POINTS

- Slow convergence in wavenumber integrals for shallow sources limits the calculation of synthetic seismograms.
- Direct convergence method accelerates convergence and achieves higher accuracy than peak-trough averaging method, only in less than 20 code lines.
- This plug-and-play algorithm enables efficient high-fidelity seismogram synthesis for challenging scenarios.

INTRODUCTION

The computation of synthetic seismograms for layered media serves as a fundamental and essential tool for researchers to understand Earth's internal structure and earthquake processes. Since the 1950s, advancements in computer technology have led to significant progress in the development of methods for calculating synthetic seismograms. Among these, the generalized reflection-transmission matrix (GRTM) method based on the discrete wavenumber method (DWM) has been widely adopted for its numerical efficiency in solving integral problems for layered media (Haskell, 1953; Kennett and Kerry, 1979; Luco and Apsel, 1983; Yao and Harkrider, 1983; Xie and Yao, 1989; Chen, 1993). However, when the source and receiver are at close depths, the integrand converges very slowly, requiring an impractically large wavenumber cutoff in DWM, which drastically reduces computational efficiency. The computation of synthetic seismograms for sources and receivers at close depths has critical applications in seismology, including monitoring induced seismicity, studying landslide dynamics, analyzing meteorite impacts, examining volcanic tremors, and monitoring nuclear explosions. To address the slow convergence, the semi-analytical method (SAM) was developed (Apsel and Luco, 1983; Herrmann and Wang, 1985; Hisada, 1994, 1995). In SAM, the integral is split into two parts: one is solved analytically, whereas the other, which benefits from the separation of the integrand, converges rapidly and can be evaluated numerically. Although

1. Key Laboratory of Deep Petroleum Intelligent Exploration and Development, Institute of Geology and Geophysics, Chinese Academy of Sciences, Beijing, China, https://orcid.org/0009-0004-7933-3357 (DZ); 2. University of Chinese Academy of Sciences, Beijing, China, https://orcid.org/0000-0002-9623-9221 (JH); 3. Key Laboratory of Planetary Science and Frontier Technology, Institute of Geology and Geophysics, Chinese Academy of Sciences, Beijing, China, https://orcid.org/0000-0002-4029-1266 (ZY)

*Corresponding author: xutao@mail.iggcas.ac.cn

Cite this article as Zhu, D., T. Xu, J. Hao, and Z. Yao (2025). A Direct Convergence Method for Computing Synthetic Seismograms for a Layered Half-Space with Sources and Receivers at Close Depths, *Bull. Seismol. Soc. Am.* **116**, 576–588, doi: 10.1785/0120250190

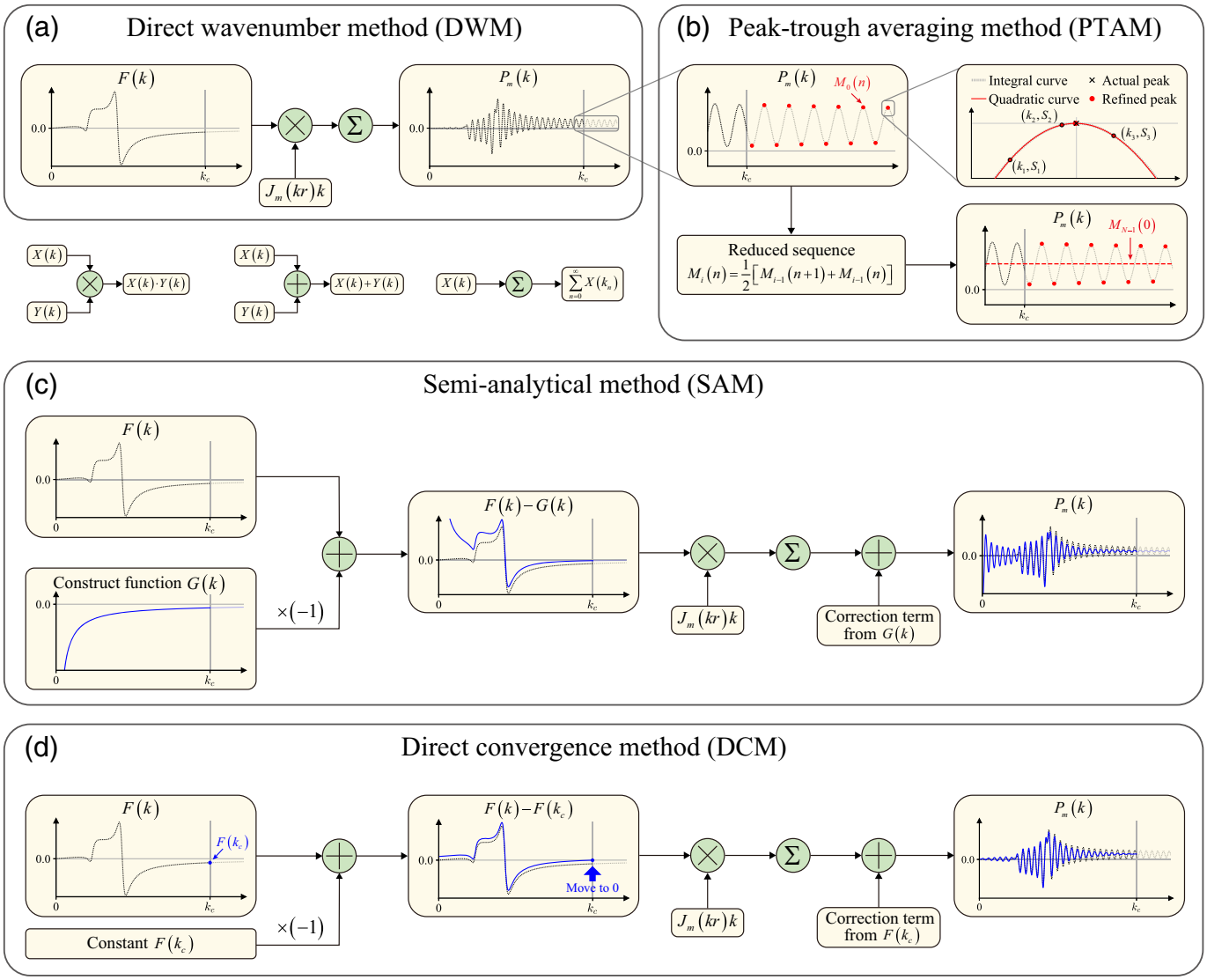

Figure 1. Schematic workflow of (a) discrete wavenumber method (DWM), (b) peak-trough averaging method (PTAM), (c) semi-analytical method (SAM), and (d) direct convergence method (DCM) for addressing slow convergence in integration. $F(k)$ is the kernel function, $J_m(kr)$ is the mth order Bessel function of the first kind, $P_m(k)$ is the integration result with upper limit k (defined in equation 4), k_c is the critical wavenumber. See the Method section for more details. The color version of this figure is available only in the electronic edition.

SAM effectively resolves the slow convergence, its mathematical treatment is cumbersome and requires a specialized numerical implementation. To reduce the complication of SAM, Greenfield (1995) developed the contour deformation method. This technique uses the asymptotic solutions of Hankel functions to obtain convergent results at large epicentral distances and has been applied to simulate strong ground motion near the fault plane in a layered half-space (Hisada and Bielak, 2003). Regarding the numerical method, Zhang *et al.* (2003) developed the peak-trough averaging method (PTAM) based on the repeated averaging method (RAM; Chang, 1988) to accelerate convergence for shallow sources. PTAM extracts peaks and troughs from the oscillatory integral to form a reduced sequence, then iteratively averages adjacent pairs to estimate the final convergence value. Compared to SAM, PTAM minimizes mathematical complexity and is more straightforward to implement numerically.

In this study, inspired by SAM and PTAM, we propose a new numerical integration method, the direct convergence method (DCM), to accelerate the convergence of wavenumber integrals. As the name suggests, DCM achieves improved convergence near the cutoff wavenumber by directly removing the slowly convergent component of the integrand through subtracting a constant term over a finite wavenumber interval, followed by adding an analytically derived correction term. Although this adjustment to the integral formula may resemble SAM in principle, DCM requires minimal mathematical complexity for implementation yet achieves high convergence accuracy. Figure 1 schematically illustrates the workflow of DWM, PTAM, SAM, and DCM for addressing the slow convergence issue. From the perspective of PTAM, DCM

implicitly extracts an infinite series of peaks and troughs and automatically estimates their convergence limit. Unlike PTAM, which relies on careful curve fitting to locate the peaks and troughs, DCM is numerically straightforward to implement, introduces negligible computational overhead, and avoids additional memory demands. This simplicity allows researchers to easily adapt existing codes for synthetic seismogram computation with shallow sources. For example, in the PyGRT package (Zhu *et al.*, 2025; see Data and Resources), we implemented DCM by adding fewer than 20 lines of code to the original DWM framework. Numerical experiments confirm that DCM produces accurate synthetic seismograms with higher convergence accuracy and stability compared to PTAM.

In the following sections, we will first provide a brief introduction to DWM, SAM, and PTAM, then describe the implementation of DCM, and finally conduct a series of rigorous comparisons and application tests.

METHOD

Basic theory

According to Yao and Harkrider (1983), solving the Green's functions for layered media in the frequency domain requires solving the following integral:

$$I_m(\omega) = \int_0^{+\infty} F(k,\omega) J_m(kr) k \, \mathrm{d}k, \quad m = 0,1,2, \tag{1}$$

in which ω is the angular frequency, k is the wavenumber, r is the epicentral distance, $J_m(kr)$ is the mth order Bessel function, and the kernel function $F(k,\omega)$ is the response of medium, which can be solved by GRTM. In this article, $F(k,\omega)$ generally denotes various types of kernel functions, whereas $g(k,\omega)$ specifically refers to the displacement kernel function, and $g_z(k,\omega)$ specifically refers to the kernel function for the derivative of displacement with respect to the receiver depth. The computation of stress, strain, and rotation tensors requires calculating the spatial derivatives of displacement with respect to the receiver coordinates. This involves replacing the displacement kernel function in equation (1) with $g_z(k,\omega)$, or replacing the Bessel function with its derivative. The resulting integral retains the same form as equation (1).

Bouchon (1981) proposed the DWM for the numerical evaluation of the integral in equation (1), expressed as

$$I_m(\omega) = \Delta k \sum_{n=1}^{\infty} F(k_n,\omega) J_m(k_n r) k_n, \tag{2}$$

in which $\Delta k = 2\pi/L$, $k_n = n\Delta k$, L is the characteristic length. Bouchon (1981) proposed that L must satisfy

$$\begin{cases} \sqrt{(L-r)^2 + |z|^2} > \alpha T \\ r < L/2 \end{cases}, \tag{3}$$

in which T is the time window length, $|z|$ is the depth gap between the source and receiver, α is the maximum P-wave velocity in the model. In practical computations, the integral in equation (1) is typically divided into two parts:

$$P_m(k,\omega) = \int_0^k F(s,\omega) J_m(sr) s \, \mathrm{d}s, \tag{4}$$

$$I_m(\omega) = \lim_{k\to\infty} P_m(k,\omega). \tag{5}$$

The integral in equation (4) can be evaluated numerically using equation (2). To approximate the limit in equation (5), an empirical critical wavenumber k_c is selected as the upper bound in equation (4), ensuring the kernel function decays sufficiently close to zero beyond this point. Following Zhu and Rivera (2002) and Zhang *et al.* (2003), we can empirically set k_c as follows:

$$k_c = \sqrt{\left(s_1 \times \frac{\pi}{|z|}\right)^2 + \left(s_2 \times \frac{\omega}{v_{\min}}\right)^2}, \tag{6}$$

in which $v_{\min}$ is the minimum velocity of the model, and s_1 and s_2 are the scale factors, which can be adjusted manually to suit specific scenarios. Unless otherwise specified, we set $s_1 = 5$ and $s_2 = 1.15$ in the following tests. With a suitable k_c, the remaining contribution to the integral is then negligible and can be safely disregarded (Zhu and Rivera, 2002; Zhang *et al.*, 2003).

When the source and receiver are at close depths, the integral in equation (1) converges extremely slowly. Figure 1a shows how the integral oscillates severely with k_c when applying DWM, necessitating an impractically large upper limit to achieve satisfactory accuracy, which severely compromises computational efficiency. To address this issue, SAM was developed by decomposing equation (1) into two terms:

$$\begin{aligned} I_m &= \int_0^{+\infty} [F(k) - G(k) + G(k)] J_m(kr) k \, \mathrm{d}k \\ &= \int_0^{+\infty} [F(k) - G(k)] J_m(kr) k \, \mathrm{d}k + \int_0^{+\infty} G(k) J_m(kr) k \, \mathrm{d}k, \end{aligned} \tag{7}$$

in which for notational simplicity, we omit the frequency parameter ω in the functions (i.e., $F(k,\omega)$ is abbreviated as $F(k)$, and $I_m(\omega)$ as I_m). Here, $G(k)$ is a kernel function constructed based on specific physical considerations, designed such that the first integral converges rapidly whereas the second admits an analytical solution. For instance, Apsel and Luco (1983) observed that the dynamic Green's functions asymptotically approach the static Green's functions (called the asymptotic solutions) as k increases. They thus approximated $G(k)$ using the static solution for a homogeneous half-space with the same material properties as the layer that includes the source. Herrmann and Wang (1985) improved upon the Apsel and Luco (1983) by employing numerical fitting with polynomial–exponential functions to derive a more accurate asymptotic approximation. Hisada (1994, 1995) further refined the GRTM proposed by Luco and Apsel (1983)

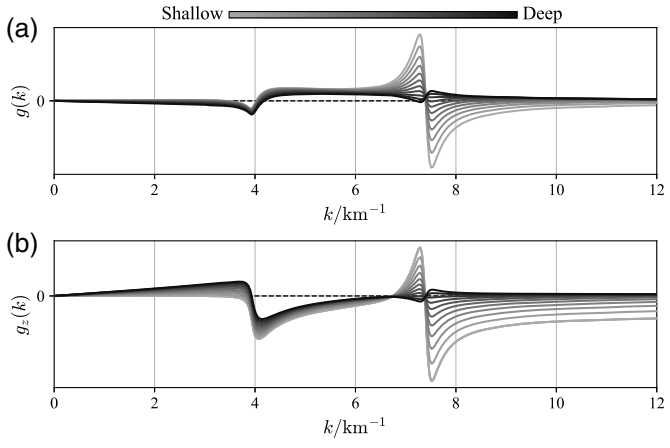

Figure 2. Morphological variations of the kernel functions (a) $g(k)$ and (b) $g_z(k)$ for the vertical displacement, with the depth of horizontal force sources varying from relatively deep (dark gray, 0.2 km) to shallow (light gray, 0 km). A half-space model (Table 1) is used. The receiver is at the surface, with an epicentral distance 10 km. The frequency is 5 Hz. Unless otherwise specified, all traces in the following figures are the real parts, and they are normalized using the maximum absolute value.

and incorporated contributions to the asymptotic solutions from direct, reflected, and transmitted waves between layers, significantly accelerating convergence. As noted explicitly by Hisada (1995), the more accurate the asymptotic solutions are, the faster the integral converges. However, this gain in efficiency comes at the cost of increased mathematical complexity and code implementation. Figure 1c shows the workflow of SAM. It can be seen that SAM effectively alleviates the integral oscillation problem existing in DWM, and the convergence speed has significantly increased.

The slow convergence issue can also be addressed using purely numerical methods. Zhang *et al.* (2003) proposed the PTAM to estimate the limit in equation (5). Figure 1b shows the workflow of PTAM. After reaching the critical wavenumber k_c, PTAM extracts consecutive peaks and troughs from the oscillatory integral curve to form a reduced sequence $M_0(n)$. The ith order reduced sequence is then defined as

$$M_i(n) = \frac{1}{2}[M_{i-1}(n+1) + M_{i-1}(n)], \quad i = 1,2,3\ldots \tag{8}$$

As $n \to \infty$, both M_i and M_0 converge to the same limit, with higher-order reduced sequences exhibiting faster convergence. The final PTAM convergence estimate is given by $M_{N-1}(0)$, in which N represents the number of extracted peaks and troughs. In practical implementation, the accuracy of PTAM's convergence estimate critically depends on accurate identification of peaks and troughs. To achieve this in discrete wavenumber sampling, Zhang *et al.* (2003) employed quadratic curve fitting using three consecutive sample points to estimate local extrema. Compared to the RAM, this approach demonstrates significantly improved accuracy.

Decay of the Kernel function

The Bessel function in equation (1) is an oscillatory function, which is the fundamental cause of the integral's oscillatory behavior. The convergence rate of the integral—that is, how the oscillation amplitude decays as k increases—depends on the decay rate of the kernel function $F(k)$ toward zero. Figure 2a illustrates the morphological changes in the displacement kernel function $g(k)$ as the source depth varies from deep to shallow. It can be observed that when the buried source is at some distance from the surface, $g(k)$ decays rapidly. However, as the source approaches the receiver at the surface, the decay of $g(k)$ slows significantly. This is the direct cause for the slow convergence of the integral.

Similar to the variation pattern of $g(k)$ shown in Figure 2a, $g_z(k)$ also exhibits slow decay characteristics (Fig. 2b). However, the decay rate of $g_z(k)$ is significantly slower than that of $g(k)$, causing the integrand in equation (1) to oscillate more irregularly. This makes it difficult for methods like PTAM to accurately compute physical quantities like stress. The decay rates of these functions can be analyzed through their asymptotic solutions. For large wavenumbers, the kernel functions approximate the following forms (Hisada, 1994):

$$\begin{aligned} g^R(k) &\approx (a_1 + a_2 k)e^{-k|z|}, \\ g_z^R(k) &\approx (a_3 + a_4 k)ke^{-k|z|}, \\ g^L(k) &\approx a_5 e^{-k|z|}, \\ g_z^L(k) &\approx a_6 ke^{-k|z|}, \end{aligned} \tag{9}$$

in which the superscript R denotes coupled P-SV waves (vertical and radial components), and L denotes SH waves (tangential component). $a_1 \sim a_6$ are constants estimated under the large-wavenumber approximation. It is evident that the long-term decay of the kernel functions is dominated by the exponential term $e^{-k|z|}$. When the depth gap $|z| \to 0$, the decay becomes extremely slow. Moreover, the asymptotic expression for $g_z(k)$ includes an additional linear factor k, which further delays its decay in the short to intermediate wavenumber range and can even cause local increases, making the corresponding integrals more challenging to evaluate.

DCM

To address the slow decay of the kernel function, DCM decomposes the integral in equation (1) into two terms:

$$\begin{aligned} I_m &= \int_0^{+\infty} [F(k) - F(k_c) + F(k_c)]J_m(kr)k\,\mathrm{d}k \\ &= \underbrace{\int_0^{+\infty} [F(k) - F(k_c)]J_m(kr)k\,\mathrm{d}k}_{I_m^{(1)}} + F(k_c)\underbrace{\int_0^{+\infty} J_m(kr)k\,\mathrm{d}k}_{I_m^{(2)}}. \end{aligned} \tag{10}$$

This decomposition resembles SAM but differs in that DCM employs a constant term $F(k_c)$, avoiding the complex

mathematical treatments required by SAM to construct asymptotic solutions. The first integral $I_m^{(1)}$ can still be evaluated using DWM by truncating the upper limit at a finite k_c and computing the numerical integral via equation (2). Although the second integral $I_m^{(2)}$ is divergent, its analytical solution can be derived under the Cauchy principal value (see the Appendix for details). The key advantage of this decomposition is that the integrand of $I_m^{(1)}$ vanishes at $k = k_c$, ensuring direct convergence of $I_m^{(1)}$ as the upper limit approaches k_c—hence the name "DCM." Meanwhile, $I_m^{(2)}$, serving as a correction term for I_m, is straightforward to implement in code due to its closed-form solution. Figure 1d shows the workflow of DCM. As shown, DCM achieves convergence during the integration phase through a simple shift of the kernel function, eliminating the need for the additional numerical computations required in PTAM.

NUMERICAL EXAMPLES

Validation

The Sommerfeld integral describes the potential of a spherical wave in an unbounded, homogeneous medium. This integral form exhibits slow convergence when the source and receiver are near the same depth—a key challenge in wave propagation modeling. Because of the availability of its closed-form solution, it is widely used to verify numerical integration techniques (Hisada, 1994; Zhang *et al.*, 2003). The Sommerfeld integral is defined as

$$\frac{e^{-ik^*R}}{R} = \int_0^\infty \frac{e^{-\gamma|z|}}{\gamma} J_0(kr)k\,\mathrm{d}k, \tag{11}$$

in which $k^* = \omega/c$, $R = \sqrt{r^2 + z^2}$, and $\gamma = \sqrt{k^2 - k^{*2}}$ with $Re\{\gamma\} \geq 0$. The exponential term $e^{-\gamma|z|}$ effectively mimics the decay of kernel functions. Because the integrand in equation (11) has a pole at k^*, following Bouchon (1981), we introduce a small imaginary component to the angular frequency ω to slightly shift the integration path away from the real axis, ensuring numerical stability.

To better validate DCM, we derive two new integrals from the original Sommerfeld potential by taking its first and second derivative with respect to r. These are expressed as

$$\left(ik^* + \frac{1}{R}\right)\frac{r}{R^2}e^{-ik^*R} = \int_0^\infty \frac{k}{\gamma}e^{-\gamma|z|}J_1(kr)k\,\mathrm{d}k, \tag{12}$$

and

$$-\left[\left(ik^* + \frac{1}{R}\right)\left(\frac{3r^2}{R^2} - 2\right) - \frac{k^{*2}r^2}{R}\right]\frac{1}{R^2}e^{-ik^*R} = \int_0^\infty \frac{k^2}{\gamma}e^{-\gamma|z|}J_0(kr)k\,\mathrm{d}k. \tag{13}$$

These derived integrals share a similar form with equation (1). Their kernel functions, $\frac{k}{\gamma}e^{-\gamma|z|}$ and $\frac{k^2}{\gamma}e^{-\gamma|z|}$, effectively capture the asymptotic behavior of $g(k)$ and $g_z(k)$ at large wavenumbers. Using the equations (12) and (13) instead of equation (11) thus offers a more thorough test of DCM's performance in computing displacements and their spatial derivatives under slow convergence.

Given that DCM and SAM share a similar integral decomposition strategy, we also evaluate SAM's performance. In SAM, using the static solution ($\omega = 0$) (Apsel and Luco, 1983), the integral in equation (12) is decomposed as

$$\int_0^\infty \frac{k}{\gamma}e^{-\gamma|z|}J_1(kr)k\,\mathrm{d}k = \int_0^\infty \left[\frac{k}{\gamma}e^{-\gamma|z|} - e^{-k|z|}\right]J_1(kr)k\,\mathrm{d}k + \int_0^\infty e^{-k|z|}J_1(kr)k\,\mathrm{d}k, \tag{14}$$

in which the second integral has an analytical solution,

$$\int_0^\infty e^{-k|z|}J_1(kr)k\,\mathrm{d}k = \frac{r}{R^3}, \tag{15}$$

and the integral in equation (13) is decomposed as

$$\int_0^\infty \frac{k^2}{\gamma}e^{-\gamma|z|}J_0(kr)k\,\mathrm{d}k = \int_0^\infty \left[\frac{k^2}{\gamma}e^{-\gamma|z|} - ke^{-k|z|}\right]J_0(kr)k\,\mathrm{d}k + \int_0^\infty e^{-k|z|}J_0(kr)k^2\,\mathrm{d}k, \tag{16}$$

in which the second integral has an analytical solution,

$$\int_0^\infty e^{-k|z|}J_0(kr)k^2\,\mathrm{d}k = \frac{1}{R^3}\left(2 - \frac{3r^2}{R^2}\right). \tag{17}$$

Figures 3 and 4 demonstrate how integrals in equations (12) and (13) are solved using DWM, SAM, and DCM. We intentionally derived the integrals in equations (12) and (13) so that the process of solving them would be analogous to computing displacements and stresses in practical synthetic seismogram simulations. Therefore, to some extent, the test in Figure 3 reflects the capability of these three methods for computing displacements, whereas the test in Figure 4 reflects their capability for computing stresses. The conventional DWM produces results that oscillate continuously, failing to converge to a stable solution. This problem becomes particularly severe when computing the integral in equation (13) (Fig. 4), for which the oscillations grow stronger, making convergence even more challenging. In contrast, both DCM and SAM employ integral decomposition—through equation (10) for DCM and equations (14)–(17) for SAM—which causes their kernel functions to decay rapidly to zero. As a result, the oscillatory behavior of the integrands is quickly suppressed. The final converged values from DCM and SAM show excellent agreement with the theoretical solution, as represented by the black-dashed horizontal lines in panel (c) of both figures.

The critical wavenumber k_c plays a central role in numerical integration methods, directly controlling both the accuracy of results and computational speed. To compare the performance of different methods, we measured how their errors relative to

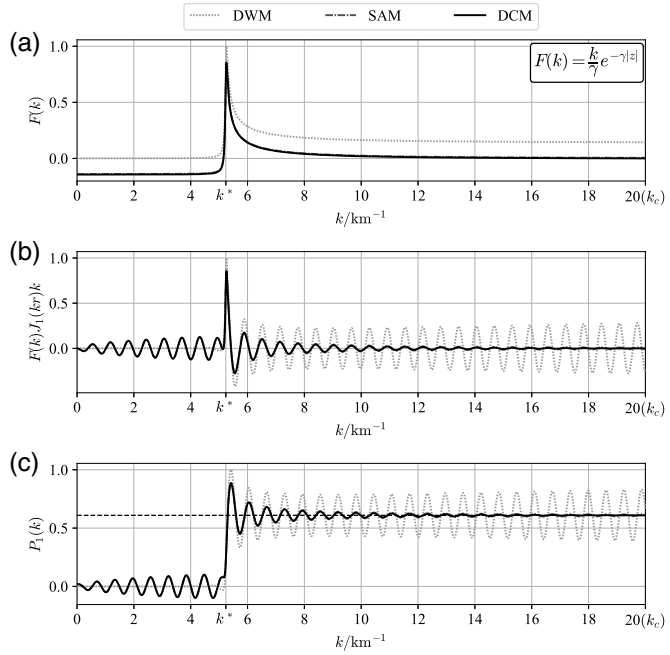

Figure 3. (a) The kernel function, (b) the integrand, and (c) the derived Sommerfeld integral in equation (12) versus wavenumber. In these panels, the curves of DCM and SAM almost overlap. The black-dashed horizontal line denotes the theoretical solution of the derived Sommerfeld integral. Here, $f = 5$ Hz, $c = 6$ km/s, $|z| = 1 \times 10^{-4}$ km, $k_c = 20$ km^{-1}, $k^* = \omega/c$, and $r = 10$ km. See the Validation section for details.

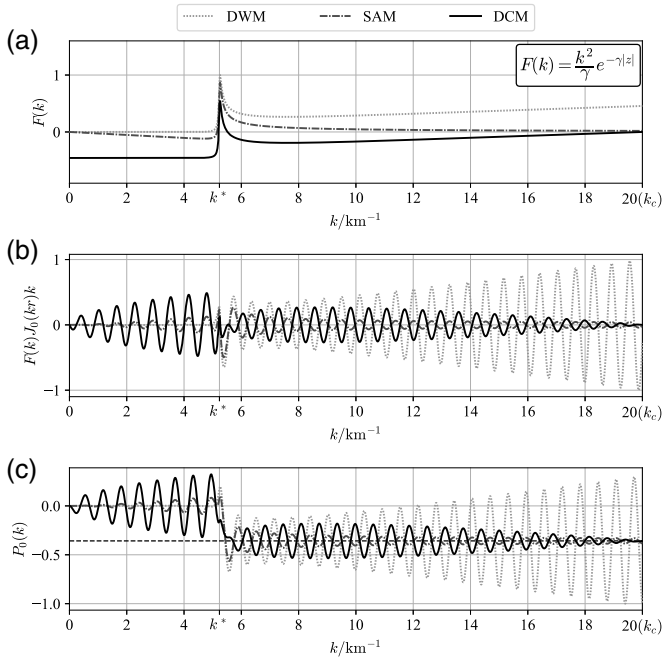

Figure 4. Same as Figure 3 but test the derived Sommerfeld integral in equation (13).

the theoretical solution change with k_c. As shown in Figure 5a, when the wavenumber exceeds a certain value ($k > k^*$), all methods initially show oscillating yet decreasing errors. However, the error for the DWM quickly levels off. The PTAM, which builds on DWM, achieves better accuracy but also stops improving with larger k_c. Although using more peaks and troughs in PTAM could reduce error further, it makes the method slower and less generally applicable. In contrast, both the SAM and the DCM maintain decreasing errors as k_c increases. Impressively, DCM achieves errors up to 100 times smaller than SAM. Figure 5b shows similar trends for a more difficult integral in equation (13). Here, errors for both DWM and PTAM even increase slightly at some points, reflecting the greater challenge of this case. Although DCM's error curve shows a small turning due to its approximation of the kernel function's decay, it still delivers the highest overall accuracy across the tested k_c range.

This test demonstrates that DCM, although employing an integral decomposition strategy similar to SAM, not only preserves SAM's advantage of rapid convergence but also achieves higher computational accuracy without requiring complex mathematical derivations.

Accuracy

To evaluate the accuracy of DCM in computing practical displacements and stresses, we applied both DCM and PTAM to solve the Lamb (1904) problem in a half-space model (Table 1). We used synthetic seismograms calculated by the Cagniard–de Hoop method (CHM; Cagniard, 1939; de Hoop, 1960; Johnson, 1974) as reference solutions ("ground truth"). Following Chen and Zhang (2001), we defined the relative error function as

$$\Phi = \frac{\int_0^T |U(t) - U^*(t)| \, \mathrm{d}t}{\int_0^T |U^*(t)| \, \mathrm{d}t}, \tag{18}$$

in which $U^*(t)$ represents the reference seismogram, and T is the length of the time series.

We began by testing how well DCM and PTAM perform when the source is placed at different depths. As shown in Figure 6a, for vertical displacements recorded at the surface, both methods become more accurate as the source gets deeper. Although their error trends look similar, DCM consistently shows smaller errors than PTAM. It is worth noting that even when the source is very shallow (0.01 km deep), both methods keep errors down to about 3%. Figure 6b compares the synthetic waveforms, showing that results from both methods match the reference solution (CHM) quite well. The main difference appears in the strength of Rayleigh waves—likely due to inherent differences between frequency- and time-domain calculation methods. This confirms that both DCM and PTAM reliably calculate ground displacements with shallow sources.

Building on the previous analysis of displacement (Fig. 6a,b), Figure 6d,e shows how well each method calculates the derivative of vertical displacement with respect to the receiver

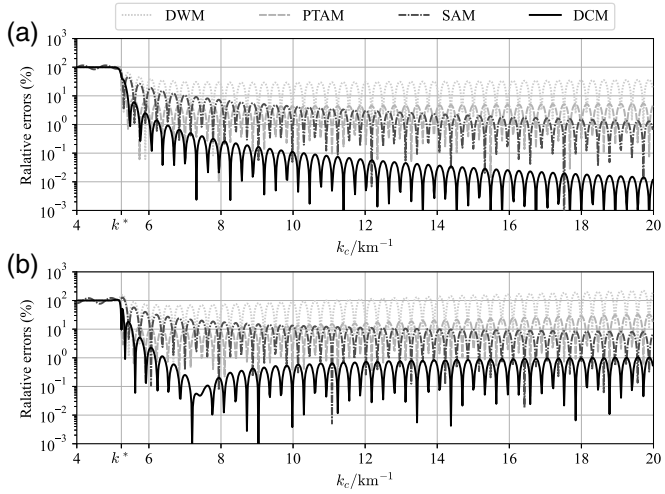

Figure 5. Relative errors between integral results of different methods and the theoretical solutions under different critical wavenumbers. The kernel function and the parameter settings are all consistent with those of (a) Figure 3 and (b) Figure 4.

depth—a key step for simulating stress. The results indicate that PTAM produces significant errors and struggles to accurately resolve near-surface stresses from a shallow source. In contrast, DCM maintains low relative errors, and its output closely matches the reference waveforms. This confirms that DCM reliably computes spatial derivatives of displacement, making it suitable for simulating related physical quantities such as stress.

The precision of the integration result is directly tied to the choice of the critical wavenumber k_c. We examined how the relative error of the 1 Hz frequency component changes as k_c varies. As seen in Figure 6c,f, the overall relative error decreases in an oscillatory manner for both methods—a pattern consistent with Figure 5. However, DCM produces lower errors with less fluctuation, showing it is less sensitive to the k_c than PTAM. In fact, when calculating the z-derivative, PTAM struggles to determine a suitable k_c at all. This confirms that DCM delivers higher accuracy alongside greater reliability.

Notably, Figure 6a reveals that both DCM and PTAM exhibit similar patterns in their relative errors. This indicates that the two methods are fundamentally guided by the same theoretical framework. In other words, both rely on the same key assumption: when $k = k_c$, the kernel function $F(k)$ has essentially converged to $F(k_c)$ (regardless of whether $F(k_c)$ equals zero), and for $k > k_c$, the kernel function $F(k)$ remains nearly constant. As a result, the integral in equation (4) oscillates symmetrically around an approximately fixed convergence value.

Under this assumption, PTAM explicitly extracts a series of peaks and troughs to compute reduced sequences, thereby achieving high-accuracy convergence estimated displacements. However, PTAM struggles when calculating stresses because the slower decay of the corresponding kernel function means the limited number of peaks and valleys no longer reliably follows the expected pattern. In contrast, DCM analytically decomposes these oscillations from the integral during the theoretical derivation phase and supplements them with a correction term derived from the integral's analytical solution. From this perspective, DCM can be viewed as implicitly extracting an infinite number of peaks and troughs while automatically estimating the convergence value. This makes DCM universally applicable for computing both displacements and their spatial derivatives. A key advantage is that DCM bypasses the need for PTAM's intricate process of numerically pinpointing peaks and troughs through curve fitting. This leads to a much simpler implementation and delivers more accurate results.

The assumption also explains the systematic variation of relative errors observed in Figure 6a,d. In practical implementations, we avoid using excessively large k_c values. Consequently, when the source and receiver depths are close, $F(k_c)$ represents merely an intermediate value in the kernel function's extremely slow decay process. The continued slow variation of the kernel function in the $k > k_c$ range still contributes to the final integral, which slightly deviates from the fundamental assumption of both methods and thus introduces errors. However, as demonstrated by the relative and absolute errors in Figure 6, this assumption does not significantly impact the results. In contrast, SAM aims to consider the contribution of the kernel function over the entire range, so it constructs an appropriate kernel function $G(k)$ with complex mathematical calculations. In practice, such errors are negligible, meaning DCM achieves greatest simplicity while sacrificing minimal accuracy.

TABLE 1
Parameters of the Half-Space Model

Thickness (km)	*P*-Wave Velocity (km/s)	*S*-Wave Velocity (km/s)	Density (g/cm^3)
∞	8.0	4.62	3.3

Efficiency

Figure 1b,d demonstrates that PTAM requires more computational steps compared to DCM and theoretically demands more execution time. To better quantify this difference, we conducted an efficiency comparison test. Figure 7 presents the execution time for computing Green's functions using DCM and PTAM at different critical wavenumbers k_c. Because the k_c as defined in equation (6) depends on frequency, we simplified the test by setting $\omega = \omega_{\max}$ in the k_c formula, ensuring a uniform wavenumber cutoff for all frequencies. For a fair comparison, we used a single-threaded version of the PyGRT program with standard optimizations (i.e., $-O$ in GNU compiler). All computations were performed on an Intel(R) Core(TM) Ultra 7 155 H processor.

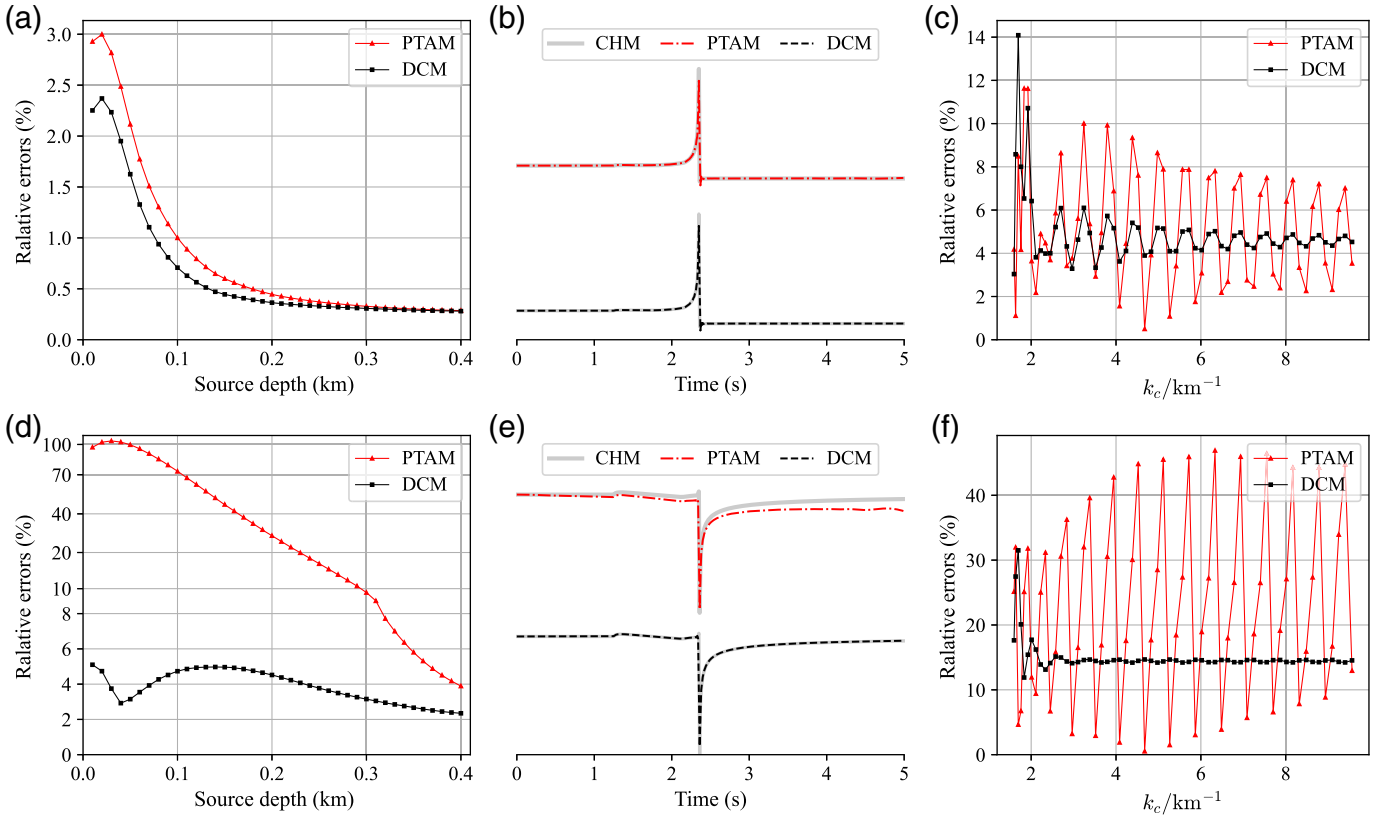

Figure 6. (a) Relative errors between the vertical displacements calculated by DCM and PTAM and the reference seismogram by the Cagniard–de Hoop method (CHM) across various source depths. (b) The waveform comparisons at a source depth of 0.01 km. (c) The relative errors of DCM and PTAM across various critical wavenumbers at frequency 1 Hz. Panels (d–f) are analogous to (a–c), respectively, but present results for the *z*-derivative of the vertical-component displacements. A half-space model (Table 1) is used. The source is a vertical downward force. The receiver is at the surface, with an epicentral distance 10 km. In panels (a–c), all traces are convolved with the step function, whereas in panels (d–f), all traces are convolved twice with the step function. The color version of this figure is available only in the electronic edition.

The results indicate that the execution time for both DCM and PTAM grows linearly with increasing critical wavenumber k_c. However, PTAM is globally slower than DCM, consistent with the operational differences illustrated in Figure 1b,d. Although modern computing technologies (including compiler optimizations and multicore processors) can substantially reduce this efficiency gap, DCM still maintains clear practical advantages. These include simpler code implementation, easier long-term maintenance, and better adaptability to different computing environments—all important factors when considering real-world efficiency.

Application

Through rigorous aforementioned testing, we have validated the correctness and computational accuracy of DCM. Next, we examine the performance of DCM under challenging physical conditions.

In earthquake engineering, near-surface velocity structures used for strong ground-motion simulation often include low-velocity, soft sedimentary layers. These layers, characterized by low density and low modulus, can significantly amplify ground vibrations due to intralayer multiples. In the first test, we computed synthetic seismograms for a sedimentary-layer model (Table 2) using both PTAM and DCM, with the source and receiver both located at the surface. The source type was a single-force point source, suitable for simulating events such as landslides, collapses, and tsunamis. As shown in Figure 8, the displacements computed by the two methods overlap well, without noticeable unphysical artifacts. The waveforms reveal that, with the source excited at the surface, the intralayer multiples within the low-velocity thin layer and the developed surface waves generate large-amplitude, long-duration coda signals, which can cause severe damage to buildings and other infrastructure. The displacement comparison demonstrates that both DCM and PTAM are capable of computing displacements in realistic low-velocity models.

Beyond the ground motion, the computed stress components are equally crucial, as they govern key engineering phenomena such as cyclic mobility in soils, foundation bearing capacity degradation, and the triggering of seismic liquefaction. Therefore, in addition to displacements, we computed all six independent components of the stress tensor. As shown in Figure 9, the three components σ_{zz},σ_{zr},$\sigma_{z\theta}$ computed by

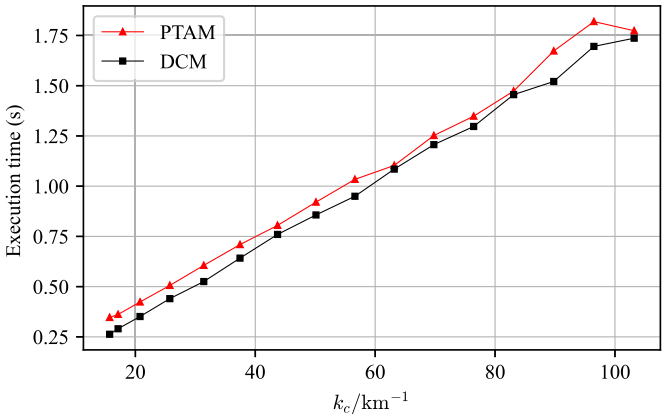

Figure 7. Execution time of DCM and PTAM at various critical wavenumbers. A half-space model (Table 1) is used. The source is at a depth of 0.01 km. The receiver is at the surface, with an epicentral distance 10 km. The number of sampling points is 1000, and the sampling frequency is 100 Hz. Each point is the average execution time of 10 repeated runs. The color version of this figure is available only in the electronic edition.

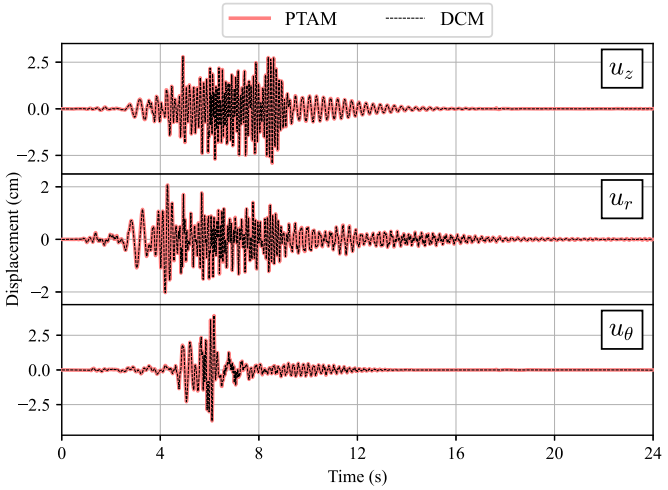

Figure 8. Comparison of the three-component displacements calculated by PTAM and DCM. A sedimentary-layer model (Table 2) is used. Both the point force ($(f_N, f_E, f_Z) = (1, 0.3, 1.5) \times 10^{15}$ dyne, defined in the north, east, and down coordinate systems) and receiver are at the surface, with an azimuth of 50° and an epicentral distance of 1 km. The sampling frequency is 50 Hz. All traces are convolved with the step function. The color version of this figure is available only in the electronic edition.

DCM remain zero over time, which correctly satisfies the free-surface boundary condition. In contrast, PTAM yields a significantly larger error in σ_{zz}. For the three nonzero components σ_{rr},$\sigma_{r\theta}$,$\sigma_{\theta\theta}$, DCM produces stable results without noticeable numerical artifacts, whereas PTAM exhibits severe nonconvergence. Figure 10 schematically illustrates the kernel functions related in Figures 8 and 9. Consistent with the earlier validation analysis based on Lamb's problem, the kernel function $g_z(k)$ decays more slowly, and its local linear variations cause unstable oscillations in the integrand, leading to PTAM's failure in stress calculations. In other words, a larger critical wavenumber k_c is required for $g_z(k)$ to enter a stable decay, forcing PTAM to sample more peaks and troughs to achieve acceptable accuracy, which in turn diminishes its advantage. As a more robust numerical method, DCM remains insensitive to the choice of k_c and its direct convergence property ensures excellent stability in the results. The stress comparison confirms that DCM serves as a reliable solution for computing stresses in realistic low-velocity models.

In the second test, we computed far-field synthetic seismograms generated by an explosion within the crustal model of

TABLE 2
Parameters of the Sedimentary-Layer Model

Thickness (km)	*P*-Wave Velocity (km/s)	*S*-Wave Velocity (km/s)	Density (g/cm^3)
0.01	1.5	0.18	1.78
0.01	1.7	0.35	1.85
0.02	1.6	0.25	1.80
0.20	2.6	1.20	2.10
∞	5.8	3.30	2.70

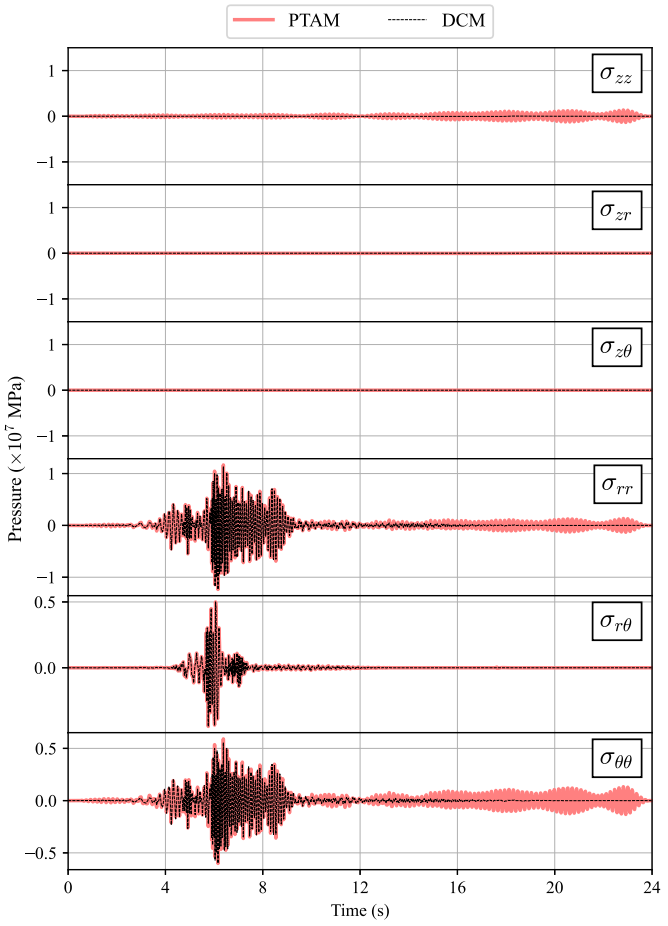

Figure 9. Comparison of the six-component stress tensor calculated by PTAM and DCM. All parameters are set the same as those in Figure 8. The color version of this figure is available only in the electronic edition.

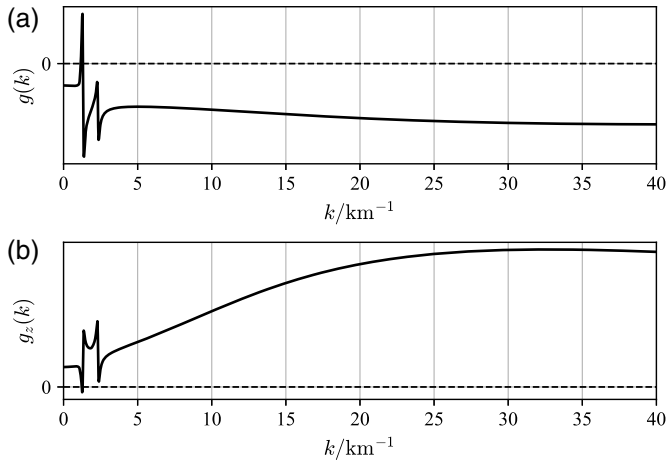

Figure 10. Kernel functions (a) $g(k)$ and (b) $g_z(k)$ for the vertical displacement. A sedimentary-layer model (Table 2) is used. Both the vertically downward force source and receiver are at the surface. The frequency is 1 Hz.

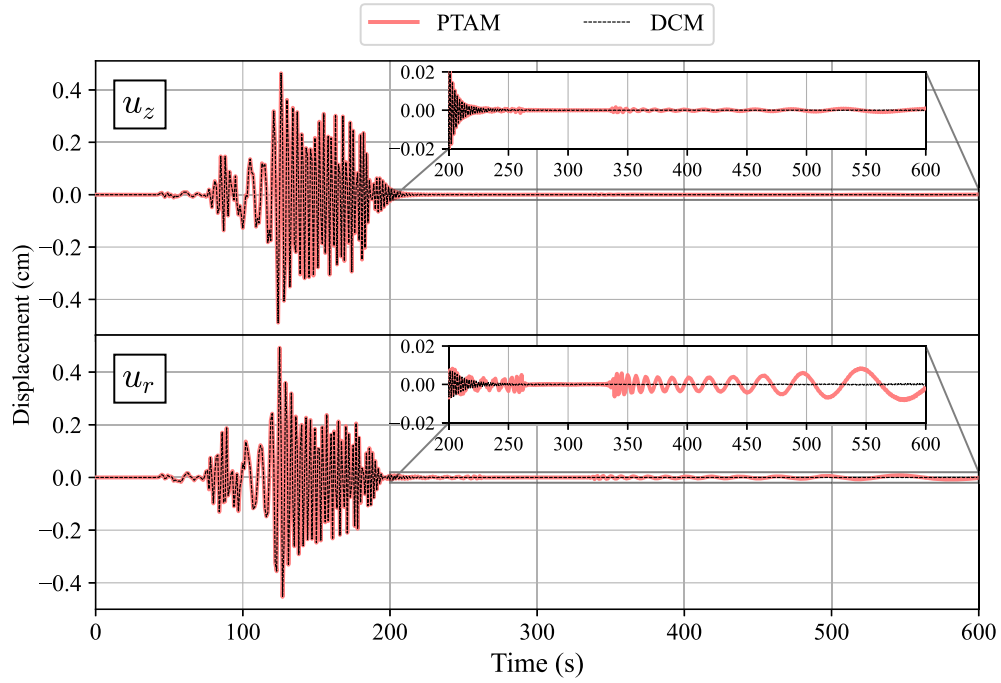

Figure 11. Comparison of the far-field displacements calculated by DCM and PTAM. The Amchitka crustal model (Table 3) is used. Both the explosion source (the scalar seismic moment $M_0 = 1 \times 10^{25}$ dyn · cm) and receiver are at the surface, with an epicentral distance of 300km. All traces are convolved with the step function. The color version of this figure is available only in the electronic edition.

the Amchitka region (Table 3). The model consists of eight layers and was used to simulate seismic recordings from the MILROW nuclear test. Both the source and the receiver are located at the surface. Because the explosive source is a dipole, the corresponding displacement can be represented by the spatial derivatives of the Green's functions with respect to the source coordinates. Consequently, the associated kernel function exhibits a decay characteristic similar to $g_z(k)$, making the solving process more challenging compared to the single-force source case. Figure 11 compares displacement results from PTAM and DCM. To avoid the low-frequency noise, in this far-field test, we set $s_1 = 0.1$ and $s_2 = 1.5$ in equation (6) and apply a high-pass filter with a corner frequency of 0.01 Hz. Although DCM produces a clean, well-converged waveform throughout, PTAM introduces significant artifacts in the coda portion where spurious oscillations reach amplitudes comparable to the body waves. Such artifacts could systematically bias subsequent analyses like signal filtering.

Besides the source type, two key factors explain the artifacts in PTAM's results (Fig. 11). First, as the epicentral distance increases, the Bessel function oscillates more rapidly. This makes it harder for PTAM's limited sampling of peaks and troughs to accurately determine the final converged value. Although using more peaks and troughs can improve accuracy, it comes at the cost of higher computational effort. In contrast, DCM remains accurate for far-field calculations because its approach depends only on the kernel function, which does not change with distance, making it unaffected by these Bessel function oscillations. Second, calculating seismograms in far-field scenarios or low-velocity models requires a longer signal duration. Equation (3) shows that this forces a very small integration step Δk. To save computation time, PTAM uses a much larger step Δk_2, based only on the epicentral distance (e.g., $\Delta k_2 = \frac{\pi}{8r}$) (Zhang *et al.*, 2003), in its stage of peak-trough collection. In this scenario, $\Delta k \ll \Delta k_2$, introducing errors into the numerical integration process. In contrast, DCM eliminates the need for PTAM's explicit second-stage convergence procedure by employing a single integration step throughout the entire integration, thereby avoiding such systematic errors.

Notably, the integration methods used in Figure 11 rely on a fixed Δk in equation (2), which becomes computationally expensive for large distances because it requires a very small Δk. To address this, Chen and Zhang (2001) developed the Self-Adaptive Filon's Integration Method (SAFIM), which dynamically adjusts the integration steps—sampling more points where

TABLE 3
Parameters of the Amchitka Crustal Model (Burdick *et al.*, 1984)

Thickness (km)	*P*-Wave Velocity (km/s)	*S*-Wave Velocity (km/s)	Density (g/cm^3)
0.2	3.4	1.7	2.3
0.6	3.7	1.9	2.4
0.5	4.2	2.1	2.4
0.5	4.6	2.3	2.5
0.7	4.9	2.8	2.6
0.5	5.1	2.9	2.7
6.0	5.9	3.3	2.7
28.0	6.9	4.0	2.8
∞	8.2	4.7	3.2

the kernel function changes rapidly and fewer where it varies slowly. This greatly improves efficiency in far-field scenarios. However, when dealing with both shallow sources and large distances, PTAM faces the same problem: it requires a separate step size during its convergence stage, which can introduce errors when combined with adaptive methods like SAFIM. In contrast, DCM's reformulation of the integral in equation (10) allows it to work naturally with SAFIM, thus avoiding such errors. Benefiting from its simplicity, DCM can be seamlessly integrated with various types of numerical techniques, establishing it as a stable, accurate, and general-purpose approach for computing synthetic seismograms from shallow sources.

CONCLUSION

The DCM effectively resolves the slow convergence of wavenumber integrals for synthetic seismograms when sources and receivers are at close depths in layered media. By decomposing the oscillatory kernel integral and analytically handling the divergent part via the Cauchy principal value, DCM eliminates the mathematical complexity of the SAM and bypasses the numerical peak-trough extraction of the PTAM. It achieves superior accuracy and stability with negligible coding effort. Rigorous validation and application tests confirm its reliability. The method's simplicity, efficiency, and seamless integration with existing codes (e.g., PyGRT) establish DCM as a general method for high-fidelity seismogram synthesis, particularly for shallow seismic sources.

DATA AND RESOURCES

The new PyGRT package with direct convergence method (DCM) was used to conduct the tests, which can be obtained at https://github.com/Dengda98/PyGRT (last accessed November 2025).

DECLARATION OF COMPETING INTERESTS

The authors acknowledge that there are no conflicts of interest recorded.

ACKNOWLEDGMENTS

The authors thank Associate Editor Martin Galis and two anonymous reviewers for their useful suggestions, which are crucial to the improvement of their article. The authors appreciate the technical support from Supercomputing Laboratory, Institute of Geology and Geophysics, Chinese Academy of Sciences (IGGCAS). This study was funded by the CAS Project for Young Scientists in Basic Research (YSBR-082) and the Deep Earth Probe and Mineral Resources Exploration-National Science and Technology Major Project (2024ZD1002905 and 2024ZD1000100).

REFERENCES

Apsel, R. J., and J. E. Luco (1983). On the Green's functions for a layered half-space. Part II, *Bull. Seismol. Soc. Am.* **73,** no. 4, 931–951, doi: 10.1785/BSSA0730040931.

Bouchon, M. (1981). A simple method to calculate Green's functions for elastic layered media, *Bull. Seismol. Soc. Am.* **71,** no. 4, 959–971, doi: 10.1785/BSSA0710040959.

Burdick, L. J., T. Wallace, and T. Lay (1984). Modeling near-field and teleseismic observations from the Amchitka Test Site, *J. Geophys. Res.* **89,** no. B6, 4373–4388, doi: 10.1029/JB089iB06p04373.

Cagniard, L. (1939). *Réflexion et réfraction des ondes séismiques progressives*, Gauthier-Villars, Paris (in French).

Chang, S. (1988). Complete wave field modeling and seismic inversion for lossy elastic layered half space due to surface force, *Ph.D. Thesis*, University of Southern California.

Chen, X. (1993). A systematic and efficient method of computing normal modes for multilayered half-space, *Geophys. J. Int.* **115,** no. 2, 391–409, doi: 10.1111/j.1365-246X.1993.tb01194.x.

Chen, X., and H. Zhang (2001). An Efficient method for computing Green's functions for a layered half-space at large epicentral distances, *Bull. Seismol. Soc. Am.* **91,** no. 4, 858–869, doi: 10.1785/0120000113.

de Hoop, A. T. (1960). A modification of cagniard's method for solving seismic pulse problems, *Appl. Sci. Res.* **8,** no. 1, 349–356, doi: 10.1007/BF02920068.

Gradshteĭn, I. S., and I. M. Ryzhik (2014). *Table of Integrals, Series, and Products*, Academic Press, London, United Kingdom.

Greenfield, R. J. (1995). Comment on "An efficient method for compouting green's functions for a layered half-space with sources and receivers at close depths" by Y. Hisada, *Bull. Seismol. Soc. Am.* **85,** no. 5, 1523–1524, doi: 10.1785/BSSA0850051523.

Haskell, N. A. (1953). The dispersion of surface waves on multilayered media, *Bull. Seismol. Soc. Am.* **43,** no. 1, 17–34, doi: 10.1029/SP030p0086.

Herrmann, R. B., and C. Y. Wang (1985). A comparison of synthetic seismograms, *Bull. Seismol. Soc. Am.* **75,** no. 1, 41–56.

Hisada, Y. (1994). An efficient method for computing Green's functions for a layered half-space with sources and receivers at close depths, *Bull. Seismol. Soc. Am.* **84,** no. 5, 1456–1472, doi: 10.1785/BSSA0840051456.

Hisada, Y. (1995). An efficient method for computing Green's functions for a layered half-space with sources and receivers at close depths (part 2), *Bull. Seismol. Soc. Am.* **85,** no. 4, 1080–1093, doi: 10.1785/BSSA0850041080.

Hisada, Y., and J. Bielak (2003). A theoretical method for computing near-fault ground motions in layered half-spaces considering static offset due to surface faulting, with a physical interpretation of fling step and rupture directivity, *Bull. Seismol. Soc. Am.* **93,** no. 3, 1154–1168, doi: 10.1785/0120020165.

Johnson, L. R. (1974). Green's function for Lamb's Problem, *Geophys. J. Int.* **37,** no. 1, 99–131, doi: 10.1111/j.1365-246X.1974.tb02446.x.

Kennett, B. L. N., and N. J. Kerry (1979). Seismic waves in a stratified half space, *Geophys. J. Int.* **57,** no. 3, 557–583, doi: 10.1111/j.1365-246X.1979.tb06779.x.

Lamb, H. (1904). I. On the propagation of tremors over the surface of an elastic solid, *Phil. Trans. Roy. Soc. Lond. A* **203,** nos. 359/371, doi: 10.1098/rsta.1904.0013.

Luco, J. E., and R. J. Apsel (1983). On the Green's functions for a layered half-space. Part I, *Bull. Seismol. Soc. Am.* **73,** no. 4, 909–929.

Xie, X., and Z. Yao (1989). A generalized reflection-transmition coefficient matrix method to calculate static displacement field of a stratified half-space by dislocation source, *Acta Geophys. Sin.* **32,** no. 3, 270–280.

Yao, Z., and D. G. Harkrider (1983). A generalized reflection-transmission coefficient matrix and discrete wavenumber method for synthetic seismograms, *Bull. Seismol. Soc. Am.* **73,** no. 6A, 1685–1699.

Zhang, H., X. Chen, and S. Chang (2003). An efficient numerical method for computing synthetic seismograms for a layered half-space with sources and receivers at close or same depths, *Pure Appl. Geophys.* **160,** 467–486.

Zhu, D., J. Wang, J. Hao, S. Yao, Y. Xu, T. Xu, and Z. Yao (2025). PyGRT: An efficient and integrated python package for computing synthetic seismograms in a layered half-space model, *Seismol. Res. Lett.* doi: 10.1785/0220250057.

Zhu, L., and L. A. Rivera (2002). A note on the dynamic and static displacements from a point source in multilayered media: A note on the dynamic and static displacements from a point source, *Geophys. J. Int.* **148,** no. 3, 619–627, doi: 10.1046/j.1365-246X.2002.01610.x.

APPENDIX

In this appendix, we will provide a mathematical derivation of the analytical expression for the integral

$$I_m^{(2)} = \int_0^\infty J_m(kr)k\ \mathrm{d}k, \tag{A1}$$

in which m is a nonnegative integer, $r > 0$, and $J_m(\cdot)$ denotes the Bessel function of the first kind of order m. The oscillatory nature of $J_m(kr)$ at infinity necessitates careful treatment to ensure convergence. Following standard regularization techniques, we introduce an exponential convergence factor e^{-ak} with $a > 0$, transforming the integral into a convergent form:

$$W_m(a) = \int_0^\infty e^{-ak} J_m(kr)k\,\mathrm{d}k. \tag{A2}$$

The original integral is recovered through the limit $I_m^{(2)} = \lim_{a\to 0^+} W_m(a)$. This regularization is justified by the fact that the Laplace transform of $kJ_m(kr)$ converges for $\mathrm{Re}\{a\} > 0$, and the limit $a \to 0^+$ yields meaningful results under conditional convergence. The derivation employs formulas from Gradshteĭn and Ryzhik (2014; hereafter, G&R) in their section 6.623, which we now reproduce verbatim.

G&R formula 6.623.1 states:

$$\int_0^\infty e^{-\alpha x} J_\nu(bx) x^\nu\,\mathrm{d}x = \frac{(2b)^\nu \Gamma\left(\nu+\frac{1}{2}\right)}{\sqrt{\pi}(\alpha^2+b^2)^{\nu+\frac{1}{2}}}, \left[\mathrm{Re}\{\nu\} > -\frac{1}{2}, \mathrm{Re}\{\alpha\} > |\mathrm{Im}\{b\}|\right]. \tag{A3}$$

G&R formula 6.623.2 states:

$$\int_0^\infty e^{-\alpha x} J_\nu(bx) x^{\nu+1}\,\mathrm{d}x = \frac{2\alpha(2b)^\nu \Gamma\left(\nu+\frac{3}{2}\right)}{\sqrt{\pi}(\alpha^2+b^2)^{\nu+\frac{3}{2}}}, [\mathrm{Re}\{\nu\} > -1, \mathrm{Re}\{\alpha\} > |\mathrm{Im}\{b\}|]. \tag{A4}$$

For $m = 0$, we apply G&R 6.623.2 with $\nu = 0$, $\alpha = a$, and $b = r$. Substituting these parameters:

$$W_0(a) = \frac{2a(2r)^0 \Gamma\left(\frac{3}{2}\right)}{\sqrt{\pi}(a^2+r^2)^{3/2}}. \tag{A5}$$

Simplifying the Gamma function $\Gamma(\frac{3}{2}) = \Gamma(1+\frac{1}{2}) = \frac{1}{2}\Gamma(\frac{1}{2}) = \frac{\sqrt{\pi}}{2}$ yields:

$$W_0(a) = \frac{2a \times 1 \times \frac{\sqrt{\pi}}{2}}{\sqrt{\pi}(a^2+r^2)^{3/2}} = \frac{a}{(a^2+r^2)^{3/2}}. \tag{A6}$$

For $m = 1$, we apply G&R 6.623.1 with $\nu = 1$, $\alpha = a$, and $b = r$:

$$W_1(a) = \frac{(2r)^1 \Gamma\left(\frac{3}{2}\right)}{\sqrt{\pi}(a^2+r^2)^{3/2}}. \tag{A7}$$

Using $\Gamma(\frac{3}{2}) = \frac{\sqrt{\pi}}{2}$ simplifies this to

$$W_1(a) = \frac{2r \times \frac{\sqrt{\pi}}{2}}{\sqrt{\pi}(a^2+r^2)^{3/2}} = \frac{r}{(a^2+r^2)^{3/2}}. \tag{A8}$$

For $m = 2$, neither G&R formula directly applies. We employ the Bessel function recurrence relation:

$$J_2(kr) = \frac{2}{kr} J_1(kr) - J_0(kr). \tag{A9}$$

Substituting into $W_2(a)$ in

$$W_2(a) = \int_0^\infty e^{-ak}\left[\frac{2}{kr} J_1(kr) - J_0(kr)\right] k\,\mathrm{d}k = \frac{2}{r}\int_0^\infty e^{-ak} J_1(kr)\,\mathrm{d}k - \int_0^\infty e^{-ak} J_0(kr) k\,\mathrm{d}k. \tag{A10}$$

The second integral is solved in equation (A6). The first integral uses G&R 6.611.1:

$$\int_0^\infty e^{-ak} J_1(kr)\,\mathrm{d}k = \frac{\sqrt{a^2+r^2}-a}{r\sqrt{a^2+r^2}}, [a > 0]. \tag{A11}$$

Combining these

$$W_2(a) = \frac{2}{r}\left(\frac{\sqrt{a^2+r^2}-a}{r\sqrt{a^2+r^2}}\right) - \frac{a}{(a^2+r^2)^{3/2}}. \tag{A12}$$

Evaluating the limit as $a \to 0^+$ for all cases:

$$\begin{aligned}
\lim_{a\to 0^+} W_0(a) &= \lim_{a\to 0^+} \frac{a}{r^3} = 0,\\
\lim_{a\to 0^+} W_1(a) &= \lim_{a\to 0^+} \frac{r}{r^3} = \frac{1}{r^2},\\
\lim_{a\to 0^+} W_2(a) &= \lim_{a\to 0^+} \frac{2r^3}{r^5} = \frac{2}{r^2}.
\end{aligned} \tag{A13}$$

Thus, the analytical expressions are

$$\begin{aligned}
\int_0^\infty J_0(kr)k\,\mathrm{d}k &= 0,\\
\int_0^\infty J_1(kr)k\,\mathrm{d}k &= \frac{1}{r^2},\\
\int_0^\infty J_2(kr)k\,\mathrm{d}k &= \frac{2}{r^2}.
\end{aligned} \tag{A14}$$

Manuscript received 4 August 2025
Published online 24 December 2025